Journal of
Synchrotron
Radiation

ISSN 0909-0495

Received 28 July 2010
Accepted 21 October 2010

X-ray analog pixel array detector for single synchrotron bunch time-resolved imaging

Lucas J. Koerner[a] and Sol M. Gruner[a,b]*

[a]Department of Physics, LASSP, Cornell University, Ithaca, NY 14853, USA, and [b]Cornell High Energy Synchrotron Source (CHESS), Ithaca, NY 14853, USA. E-mail: smg26@cornell.edu

Dynamic X-ray studies can reach temporal resolutions limited by only the X-ray pulse duration if the detector is fast enough to segregate synchrotron pulses. An analog integrating pixel array detector with in-pixel storage and temporal resolution of around 150 ns, sufficient to isolate pulses, is presented. Analog integration minimizes count-rate limitations and in-pixel storage captures successive pulses. Fundamental tests of noise and linearity as well as high-speed laser measurements are shown. The detector resolved individual bunch trains at the Cornell High Energy Synchrotron Source at levels of up to 3.7×10^3 X-rays per pixel per train. When applied to turn-by-turn X-ray beam characterization, single-shot intensity measurements were made with a repeatability of 0.4% and horizontal oscillations of the positron cloud were detected.

Keywords: time-resolved measurements; area detector; pump–probe; hybrid pixel detector.

1. Introduction

Synchrotrons are pulsed X-ray sources that may be exploited for time-resolved experiments. Isolation of the synchrotron pulses allows for dynamic studies limited by the X-ray pulse width of around 50 ps (DeCamp *et al.*, 2005). Mechanical chopper systems have been designed to transmit one X-ray pulse at a duty cycle of around 1 kHz (Cammarata *et al.*, 2009). When synchronized to a laser pump, choppers allow conventional X-ray detectors to be used for ultrafast experiments. However, detectors that isolate successive X-ray pulses from the synchrotron under control of electronic gate signals ease the experimental design and allow for a wider range of experiments. Experiments that detect spontaneous sample changes and then trigger image capture become possible with detector-based electronic shuttering. Examples include studies of crack propagation or translating reaction fronts.

Single-bunch pump–probe experiments have used point avalanche photodiodes (APD) coupled to counting external electronics to measure up to one X-ray per pulse (Baron *et al.*, 1997). The output of an APD may also be processed by analog electronics and then digitized to isolate successive X-ray pulses with a signal capacity over 500 X-rays per pulse (Cheong *et al.*, 2004). Pilatus, a photon-counting pixel array detector (PAD), was applied to single-bunch experiments at the Advanced Photon Source (APS) (Ejdrup *et al.*, 2009). To do so, the in-pixel counter of Pilatus was gated by an external control signal for isolation of single pulses at a count rate of one X-ray per pixel per pulse. Image intensifiers with a gate mode as short as 3 ns have been included in the optical chain of an X-ray CCD detector to isolate a single X-ray pulse (Nüske *et al.*, 2010). The detectors described above have limitations for high-speed experiments that analog integrating pixel array detectors may address. APDs are single pixel, digital PADs are limited in count rate and subsequently accuracy per shot, and the two-dimensional area detectors discussed above cannot isolate and record successive synchrotron pulses.

Analog integrating pixel array detectors that isolate synchrotron pulses will allow for new paradigms of single-bunch X-ray experiments and more efficiently acquire data from conventional pump–probe configurations. An analog integrating PAD is shown in this paper to measure 1000 s of X-rays per pixel per pulse for single-shot Poisson limited accuracies at each pixel of 3% or better. In-pixel frame storage captures a number of images in rapid succession before detector readout to particularly benefit the study of samples with spontaneous non-reversible changes (Trenkle *et al.*, 2008).

Analog integrating PADs are also being designed for X-ray laser sources when the signal arrives in femtoseconds. A PAD is in development for the Linac Coherent Light Source (Koerner *et al.*, 2009*a*). An integrating PAD, similar in architecture to the one presented here, that features adaptive gain is being developed for the European XFEL (Henrich *et al.*, 2010).

The detector consists of a 16×16 pixel CMOS integrated circuit hybridized to a high-resistivity silicon detector. The hybrid was combined with support electronics and flexible field-programmable gate array (FPGA) control and acquisi-

tion to create an X-ray camera. The support electronics and FPGA code allowed for a minimum exposure time of 30 ns with 10 ns resolution, a 600 µs readout and buffering for 8100 frames before a transfer to hard disk was required. The fundamental detector metrics of noise and linearity are presented.

2. Device description

The CMOS readout application-specific integrated circuit (ASIC) is a 16 × 16 pixel array with 150 µm pitch designed in the TSMC 0.25 µm process and submitted to MOSIS as part of a multi-project wafer run. The circuit layout allowed for a smaller pixel pitch but 150 µm was chosen to allow for hybridization to available detector layers. All NMOS transistors were designed using either an enclosed layout (Anelli *et al.*, 1999) or radiation-hardened linear techniques (Snoeys *et al.*, 2002). The array was divided in half; one side matched an earlier prototype while the other side implemented a few slight design modifications to address issues revealed during testing of an earlier prototype chip (particularly radiation robustness) (Koerner *et al.*, 2009). The chip has four analog output ports.

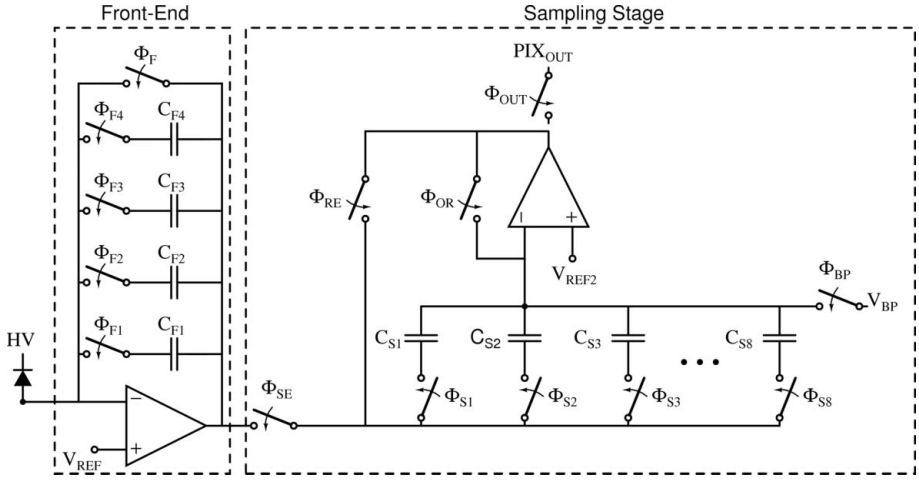

Figure 1
Simplified pixel schematic that differentiates the front-end stage and the sampling stage. The reversed biased diode represents the high-resistivity detector layer.

The pixel electronics, shown as a simplified schematic in Fig. 1, are similar to the analog integrating approach with in-pixel storage used in past detectors (Rossi *et al.*, 1999; Ercan *et al.*, 2006). The design has been updated with an emphasis on speed for bunch segregation at the 150 ns level. The in-pixel amplifiers use a differential architecture for radiation hardness and to limit systematic effects at high input X-ray flux. The front-end capacitors (C_{F1}–C_{F4} in Fig. 1) may be re-addressed and signal added without reading out the device. This addition of signal may occur after either acquisition into a different capacitor or electronic shuttering of the X-ray signal. Each in-pixel frame (a value stored onto C_{S1}–C_{S8}) may be built from temporally separated acquisition windows which allows for in-pixel averaging. Each distinct temporal window during an exposure is referred to as an accumulation.

Switches Φ_{F1}–Φ_{F4} may be held fixed to bypass accumulation. In this case, referred to as flash mode, the pixel captures eight sequential images that are stored on C_{S1}–C_{S8} before readout. The front-end conversion gain, when accumulation is not used, is set by the configuration of switches Φ_{F1}–Φ_{F4} and adjustable by a factor of up to 6.5. Pixels have four accumulation elements (C_{F1}–C_{F4}) and eight storage elements (C_{S1}–C_{S8}).

ASICs were hybridized to high-resistivity silicon detector layers. The detector layers were *n*-type 500 µm-thick layers fabricated by SINTEF (Oslo, Norway) with a gold pad metallization. Pixel *p*+ implants were at the bump-bonded side and an aluminized *n*+ ohmic contact was on the X-ray incident side for the application of a bias to deplete the thickness of the sensor. A substrate of 7.5 kΩ cm resistivity and a reverse bias of 250 V gives an anticipated hole collection time of 25 ns. With a larger overbias the minimum collection time, constrained by the hole saturated velocity, is 8.3 ns.

To bump-bond the detector layers to ASICs a process compliant with diced chips returned from MOSIS multi-project wafer runs was required. Gold stud bump bonding with conductive adhesives was used since it is compliant with small diced chips (Polymer Assembly Technologies, NC, USA). Gold stud bumps were attached to the aluminium pad on the ASIC chip by intentionally removing the wire from a thermosonic wirebond to leave only the ball-bond. A conductive polymer epoxy bump was placed on the pads of the detector through a stencil screen (Clayton *et al.*, 2003).

An FPGA board (XEM3050 Opal Kelly, Portland, OR, USA) with a Xilinx Spartan-3 FPGA was used to send digital control signals to the PAD, to buffer data from analog-to-digital converters, and to transfer data to a computer. The FPGA board featured a USB 2.0 interface for download of the FPGA configuration and for writing of exposure commands from a computer to registers in the FPGA. The FPGA system continuously read up to 8100 frames from the PAD by buffering onto a memory chip before a USB transfer to a computer was required. The exposure and reset times were determined by the FPGA and programmable from 30 ns to 21.4 s with a master FPGA clock of 10 ns.

Detectors were packaged in ceramic pin grid array (PGA) carriers. PGAs were mounted into a zero-insertion-force (ZIF) socket with a central hole that allowed a copper heat-sink to contact the back side of the PGA. The temperature of the copper heat-sink was regulated by a thermoelectric device and an RTD sensor. A support printed circuit board (PCB), detector enclosure and the FPGA board are shown in Fig. 2. The enclosure allowed for evacuation of the detector environment to prevent condensation when the detector was cooled. Electrical signals were transmitted into the enclosure through inner layers of the PCB.

3. Fundamental metrics, laser measurements and radiation hardness

3.1. Fundamental detector specifications

The RMS equivalent noise charge of the modified half of a hybridized PAD for flash-mode operation was measured at 291 K to be 1000, 1445, 2800, 3415 and 5500 e^- for capacitive feedback configurations of 300, 466, 966, 1200 and 1966 fF, respectively, by engaging combinations of switches Φ_{F1}–Φ_{F4}. Therefore, a signal-to-noise ratio of 2.2 for the detection of a single 8 keV X-ray is possible at the highest front-end gain setting. The noise of the other half, owing to differences in the sampling stage, was around 20% greater. The reported noise is the entire system noise which includes all on-chip and off-chip buffers and the ADC system. The pixel and readout chain do not have electronics for correlated double sampling as the dominant noise source has been found to be sampling onto the in-pixel storage capacitors which cannot be removed by difference measurements. The measurements used a 2 µs integration time. The PAD was measured to swing 1.88 V with a non-linearity of less than 1%. At the lowest gain the per-pixel well depth for less than 1% non-linearity is 10480 X-rays of 8 keV energy.

The calibration from V to keV was made assuming the as-drawn integration capacitor values and 100% charge collection efficiency. These assumptions were verified by collection of a single-photon spectrum with Cu *Kα* radiation and the detector in the highest gain-mode. The conversion factor was further monitored by photon-transfer-type calculations on X-ray data. Future work will develop procedures for calibrating pixel-to-pixel variations owing to readout pixel gain variations and to variations in the pixel collection area from detector layer inhomogeneities.

3.2. High-dose-rate laser measurements

The PAD linearity was studied at high input photocurrents using a laser of 633 nm wavelength, 2.3 µm absorption length in silicon (Wong, 1996) and 0.5 mW maximum output power (Melles Griot, Albuquerque, NM, USA; model 25-LHP-213-249). For efficient visible detection the aluminium on the X-ray entrance side was removed from one of the detector chips. Fig. 3 shows the integrated intensity in the laser spot *versus* the exposure time acquired at two levels of incident intensity. This result confirms the linearity of the detector system at submicrosecond exposure times.

The total photocurrents measured were 243 µA and 20 µA for direct laser illumination and attenuation with a filter of optical density 1.0. The maximum per pixel photocurrent was 12 µA without attenuation, which is comparable with the static bias current of the front-end amplifier, and the response remains linear. The photocurrent produced by the unattenuated laser is equivalent to the signal from an 8 keV X-ray flux of 7×10^{11} X-rays s^{-1}, around a factor of 1000 greater than what is accessible with laboratory X-ray sources. The largest single pixel flux, equivalent to 3.4×10^{10} X-rays of 8 keV energy, exceeded the maximum pixel count-rate (10 MHz) of area digital PADs by over 3000. The intercepts of

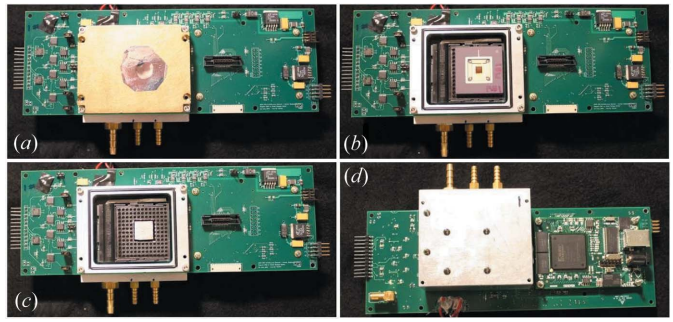

Figure 2
Photographs of the support PCB and enclosure from different angles and at different levels of construction. (*a*) The system entirely assembled from the top side. An X-ray-transparent aluminized Mylar window covers a hole in the top brass cover. The three barbed hose-fittings are a vacuum port and connections for cooling water. (*b*) The enclosure with the brass cover removed to reveal the PGA and chip mounted in the ZIF socket. (*c*) The chip is removed to show the copper cold-finger that protrudes through the ZIF socket. (*d*) PCB photographed from the back side so that the control FPGA board is shown on the right. The support PCB measured 8.0 inch × 2.85 inch.

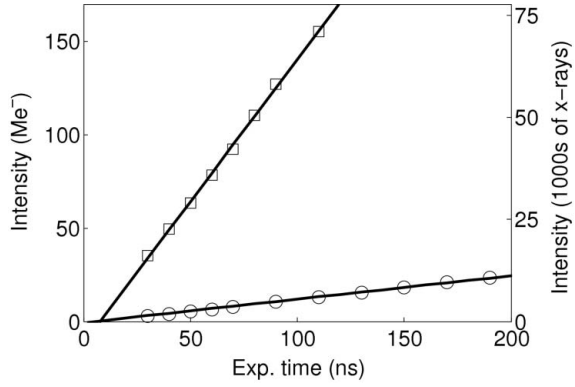

Figure 3
Detector linearity at nanosecond exposure times tested with a laser source. Squares: laser unattenuated. Circles: neutral-density filter of optical density 1.0. Solid lines are a linear fit to the measured points. Equivalent X-rays are in terms of 8 keV.

Fig. 3 were near to zero; the deviation may be because the effective exposure time was slightly different than what was programmed into the FPGA.

A laser (Newport Corp., Irvine, CA, USA; model LQA635-03C) with analog modulation at up to 20 MHz, a wavelength of 635 nm and a maximum output power of 3 mW was used to illuminate the detector with a 40 ns pulsed input to test high-speed collection. A delay generator (Stanford Research Systems, Sunnyvale, CA, USA; model DSG 535) controlled the delay between laser pulse and PAD acquisition. Data were acquired with a 90 ns exposure time, C_F = 1000 fF and with a front-end amplifier dissipation of 12.3 µA. Fig. 4 shows the integrated intensity in the detected laser spot *versus* the delay between the laser pulse and the start of the PAD exposure window (T_D) acquired at multiple values of the detector layer bias. At larger T_D the PAD was started later with respect to the laser. At bias voltages of 280 and 230 V the integrated intensity reaches a maximum and remains constant

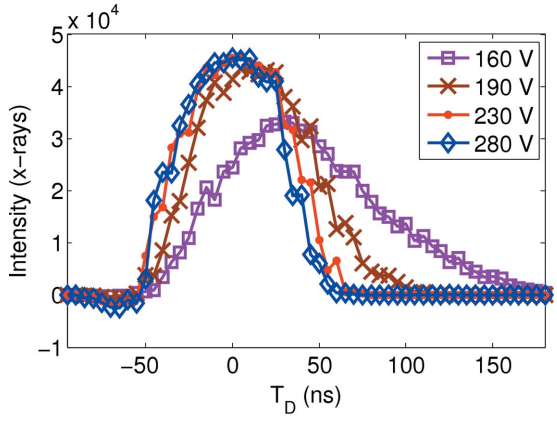

Figure 4
Integrated intensity in a detected laser spot (in equivalent 8 keV X-rays) for a laser pulse of 40 ns duration *versus* the delay between PAD acquisition and the pulse. The experiment was repeated at multiple values of the detector layer bias (HV in Fig. 1), indicated in the legend. Lines are a guide to the eye.

versus T_D for 30 to 40 ns at T_D greater than -10 ns. This indicates that the signal was completely measured in the 90 ns exposure window when the PAD was started at the appropriate time with respect to the laser, 10 ns before the laser start or up to 20 ns after the laser start. In separate experiments a longer detector exposure time was used and the same maximum intensity was measured which corroborates our claim that the laser pulse was fully measured by a 90 ns exposure time.

From the given detector resistivity it is anticipated that the detector is fully depleted at 190 V but the electric field is not sufficient for prompt charge collection. The measurement shown in Fig. 4 at 190 V compared with those at 230 and 280 V emphasizes the advantage of biasing beyond that needed for full depletion. At 160 V it is expected that the detector is not fully depleted.

3.3. Accumulation studies

The noise per accumulation was studied for multiple values of feedback capacitance. The noise measured was differentiated into two sources by a fit to $\sigma(N)^2 = \sigma_F^2 + N\sigma_{acc}^2$, where σ is the total noise measured, σ_F is the fixed noise, σ_{acc} is the noise added per accumulation and N is the number of accumulations. The noise per accumulation was found to follow the form $[(kTC_F)^{1/2} + (kTC_{IN})^{1/2}]/C_F$ where C_F is the feedback capacitance and C_{IN} is the input capacitance owing to the detector layer and input amplifier. Table 1 shows the fixed read-noise and noise per accumulation extracted from the data fits from the modified half of a hybridized detector. Also shown is the number of accumulations possible before the added accumulation noise matches the fixed read-noise.

The switches involved in accumulation were designed with dummy pairs to reduce charge injection. The largest magnitude of charge injected for the 466 fF and 500 fF feedback capacitors was 4 fC, which means that the charge injected per accumulation encompassed 0.6% of the full well. The maximum percentage of the full well per accumulation with the 300 fF feedback capacitor was 1.3%. For most measurements subtraction of a dark image acquired using the same number of accumulations is sufficient to account for the charge injected per accumulation. More detailed calibration techniques are described by Koerner (2010).

Table 1
Noise measured from accumulations differentiated as fixed noise and noise per accumulation.

The fourth column shows the number of accumulations until accumulation noise matches the fixed noise.

C_F (fF)	σ_F (μV)	σ_{acc} (μV)	N for $\sigma_F^2 = N\sigma_{acc}^2$
300	550	186	9
466	496	133	14
500	490	127	15
700	473	96	24
1666	452	42	117

The accumulation functionality allows measurement of a repetitive signal with less noise than other methods by allowing for in-pixel averaging (see the fourth column of Table 1). To demonstrate this the detector was illuminated with a laser (Coherent Laser, Santa Clara, CA, USA; Lab Laser MVP/VLM2) modulated with a sinusoid at 25 kHz. The light intensity was attenuated by 10000 using a neutral density filter for low signal level imaging. Four accumulation elements captured the intensity at four phases of the oscillation: 0°, 90°, 180°, 270° with the laser at full intensity at 90° and off at 270°. Two methods of imaging this scene were compared. One technique captured each phase of the oscillation once with an exposure time of 200 ns and then the image was read out. Fifteen of these images were averaged to form a composite image. The second technique used the four accumulation elements to capture each phase of the oscillation with a 200 ns exposure window 15 times before the detector image was read out. For this second technique the intensity was calculated from one single image rather than an average. In both cases the total exposure time for the capture of each phase of the oscillation was 15 × 200 ns = 3 μs. The first technique used post-processing averaging while the second technique averaged in-pixel. The integrated intensity measured, in units of 8 keV X-rays per pixel, along with error bars of $\pm 1\sigma$ are shown in Fig. 5. The error bars are from the error of each readout in the case of the accumulation method and are from the error of the averaged measurements in the case of post-acquisition averaging. In this experiment the number of accumulations was such that the added accumulation noise is near to that of a single readout. Hence, the noise increase expected from 15 image reads compared with a single read and 15 accumulations is $(15/2)^{1/2} = 2.7$. The ratios of the noises measured were 2.7, 2.4, 2.5 and 3.5, in reasonable agreement with expectations.

The feedback capacitors used, from left to right in Fig. 5, were 700, 300, 500 and 466 fF. The anticipated noise dependence on feedback capacitor may be estimated by application of the data in Table 1 to the noise equation $\sigma(N)^2 = \sigma_F^2 + N\sigma_{acc}^2$.

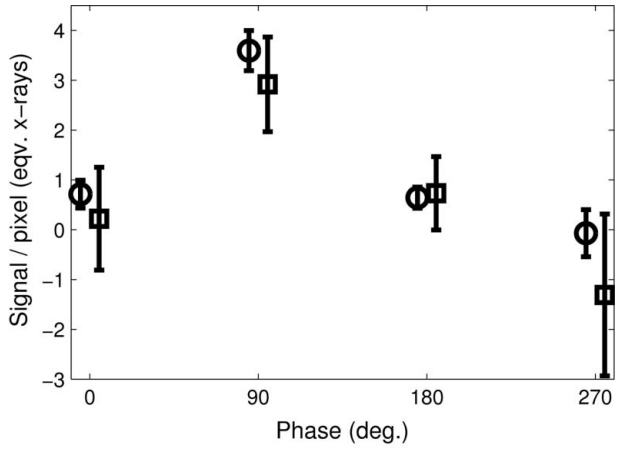

Figure 5
Signal per pixel (in equivalent 8 keV X-rays) captured at four phases of an oscillatory stimulus. Squares: data averaged in post-processing. Circles: data acquired using the accumulation functionality, *i.e.* averaged in pixel. The circles (squares) are offset horizontally by -5° ($+5^\circ$) for easier visualization.

3.4. Radiation hardness

Radiation robustness was evaluated by dosing an ASIC without a bump-bonded detector layer held at 249 K at a rate of 2 Gy(Si) s^{-1}. X-rays were produced by a rotating anode source (Enraf-Nonius, Model FR571; Bohemia, NY, USA) operated at 40 kV and 50 mA with multilayers (Osmic model CMF15-165Cu8; Troy, MI, USA) to select 8 keV radiation. The chip was irradiated up to 600 kGy(Si) over the course of three days. With a 500 µm-thick silicon detector layer for protection, a dose of 600 kGy(Si) at the readout ASIC is reached after exposure to a flux of 3×10^{11} X-rays s^{-1} mm^{-2} for 94 h at 8 keV [$\sim$800 MGy(Si) at the detector diode layer] or 77 min at 12 keV [$\sim$5.5 MGy(Si) at the detector diode layer]. The half of the chip that was modified for improved radiation hardness remained functional up to 600 kGy(Si).

The most significant effect induced by dose was a manageable increase in the sub-threshold leakage of the transistor switches that isolate the storage element capacitors. The leakage from in-pixel storage elements that were not dosed was measured at around 2 fA, which implies a droop equivalent to 0.4 X-rays of 8 keV energy given a 10 ms readout time. All NMOS transistors acting as switches were designed as enclosed layout transistors (Snoeys *et al.*, 2002), yet after dosing to 600 kGy(Si) the leakage from storage capacitors increased to up to 160 fA, which would produce a droop of 18 X-rays of 8 keV energy. This leakage was too small to be due to activation of parasitic sidewall transistors and has been attributed to a shift in the NMOS transistor threshold voltage which increased sub-threshold leakage. In this experiment the detector was cooled to 249 K to reduce the droop of storage elements. The leakage from front-end feedback capacitors was found to be noticeably less than the storage elements since the switches for accumulation were a single PMOS device whereas the storage switches were required to be a transmission gate of an NMOS and PMOS device in parallel.

4. Synchrotron measurements

4.1. High-flux studies

The high-flux X-ray performance of the detector was tested at hutch G3 of the Cornell High Energy Synchrotron Source (CHESS). CHESS G-line receives X-ray radiation from positrons *via* a 49-pole wiggler. X-rays of 8.6 keV energy were selected by a W/B_4C multilayer monochromator with energy bandpass $\Delta E/E = 2.1\%$. G3 receives a flux of up to 5×10^{13} X-rays s^{-1} mm^{-2}. In the hutch a pair of slits was used to reduce the size of the beam to around 1 mm^2. An aluminium disc with different thicknesses at each position of rotation was used to attenuate the X-ray beam when necessary. A fast shutter with $\sim$5 ms opening and closing times was used to limit X-ray exposure to the detector (Uniblitz/Vincent Associates, Rochester, NY, USA). The synchrotron timing signal triggered a delay generator which subsequently triggered the PAD. The time from arrival of the synchrotron trigger to release of the trigger to the PAD (referred to as T_D or PAD delay) and the repetition rate of exposures were adjusted with the delay generator. The detector layer was biased to 290 V and the PAD temperature was stabilized at 258 K or 249 K. PAD readout required around 600 µs.

The synchrotron positron fill-pattern during this experiment is shown in the schematic of Fig. 6 and demonstrated with a detector readout in Fig. 7. Five bunch trains circulated the ring with a front-to-front spacing of 280 ns (*A* in Fig. 6). The trains contained five or six bunches separated by 14 ns. The intra-train bunch spacing was too short to resolve so the trains were used as a stand-in for a bunch.

Fig. 7 shows that the capture of the second and third trains contained more signal than that of the first, fourth and fifth trains. The fill pattern had six bunches in the second and third trains and five bunches in the other trains. For the acquisition of Fig. 7, the detector measured an integrated intensity of 1.75×10^5 X-rays for the two bright trains and 1.44×10^5 X-rays for the other trains (a ratio which approximately matched that of the number of bunches: $1.22 \cong 6/5$).

The experiment displayed in Fig. 7 was repeated while the PAD delay (T_D) was adjusted with respect to the synchrotron timing to study the dependence of the PAD response upon the time within the exposure window that the X-rays arrived. As the PAD delay was increased the X-rays arrived earlier in the exposure window. Fig. 8 shows the integrated intensity of each storage element from a single pixel plotted *versus* the PAD delay. The group of peaks at smallest PAD delay show that C_{S2}, C_{S5} and C_{S6} measured the lower intensity bunch trains (1, 4 and 5); C_{S3} and C_{S4} measured the high-intensity trains (2 and 3); and C_{S1}, C_{S7} and C_{S8} were not illuminated. The duration of the rising and falling edges and the flat tops of the pixel response in Fig. 8 provide information about the speed of the detector response. For trains with six bunches the rising, flat-top and falling edge durations were 100 ns, 60 ns and 100 ns, respectively. For the trains with five bunches the rising, flat-top and falling edge durations were 90 ns, 75 ns and 85 ns, respectively. The total time that signal was detected was 250 ns for the five-bunch trains and 260 ns for the six-

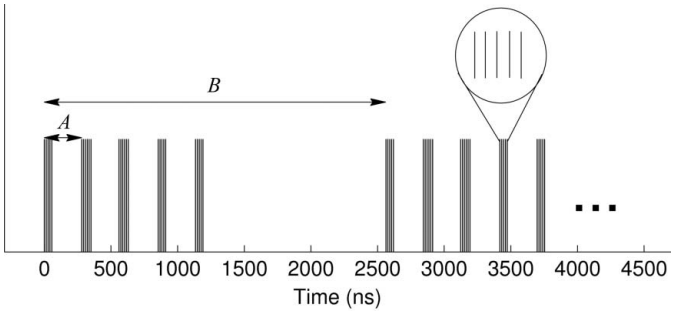

Figure 6
The five trains of bunches as each circulates the synchrotron at CHESS twice. Each individual vertical bar is a bunch of positrons. The trains, from left to right, are referred to as 1–5. Trains 2 and 3 had six bunches and trains 1, 4 and 5 had five bunches. The front-to-front train spacing was 280 ns (labeled *A*). The revolution period was 2563.2 ns (labeled *B*). The time between bunches in a train was 14 ns.

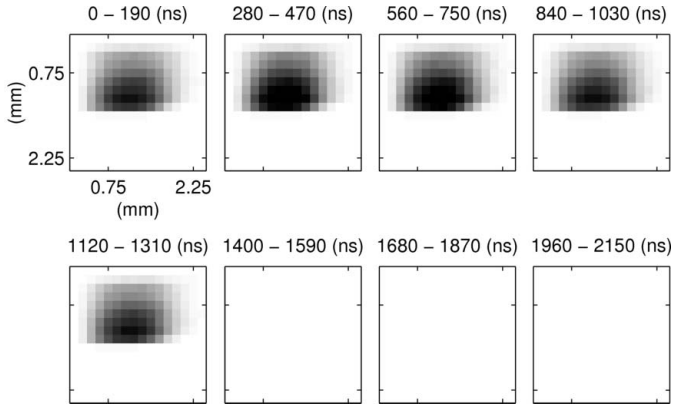

Figure 7
Eight images, one from each in-pixel storage element, acquired in a single readout to illustrate the synchrotron fill-pattern. The linear gray-scale is set from −1 X-ray (white) to 3.7 × 10^3 X-rays (black). The time window, 190 ns in duration, covered by each in-pixel storage element is labeled above the image. Time window 0–190 ns captured train 1, trains 2–5 were captured in the next successive time windows, and the last three time windows captured the period without X-rays (1200–2560 ns in Fig. 6). The sharp edge at the bottom of the spot is hypothesized to be due to vignetting from upstream optical elements.

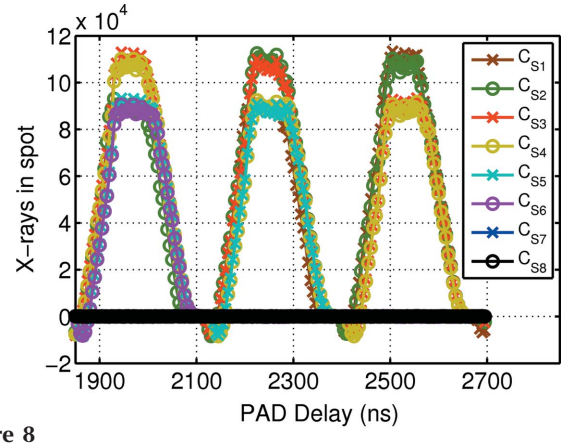

Figure 8
Integrated signal *versus* the PAD delay with respect to the synchrotron timing with a train imaged by successive in-pixel storage elements. The exposure time was 190 ns and the time between frames was 90 ns. C_{S7} and C_{S8} measured around zero at all PAD delays and are indistinguishable in the figure. Lines are a guide to the eye.

bunch trains, which is approximately the sum of the exposure time, X-ray train duration and the detector collection time which indicates that the readout ASIC electronics did not considerably slow the response. Trains are clearly separated and trains of five bunches and of six bunches are distinguishable.

The results of Fig. 8 (and Fig. 4) indicate the feasibility of isolation of single bunches with around 150 ns spacing, which is sufficiently fast for single-bunch imaging at the APS and European Synchrotron Radiation Facility (ESRF) (153 ns and 176 ns separation, respectively). The flat-top time in Fig. 8 of 75 ns suggests that at CHESS the entire signal from the train would still have been measured if the exposure time was reduced from 190 ns to 115 ns. Further, at CHESS, the rising and falling edges of Fig. 8 are slowed by the duration of the trains, whereas a single bunch is effectively a delta-function impulse at the detector. The reduction of the signal duration by 56 ns should allow reduction of the exposure time by at least 25 ns. Therefore, it is estimated that bunches at the APS could be resolved with an exposure time of 90 ns and a time between frames for pixel reset of 60 ns.

The results shown in Fig. 8 were used to evaluate the shift of the detector pedestal level and read-noise induced by high levels of X-ray flux. The time-averaged flux at the brightest pixels was measured to be 4.8 × 10^3 X-rays pixel^{-1} μs^{-1} equivalent to 2.1 × 10^{11} X-rays mm^{-2} s^{-1}. At PAD delays of 2550–2600 ns storage elements C_{S5} through C_{S8} should have measured zero. The read-noise of these, nominally empty, storage elements showed an insignificant maximum increase of 1.2% at the highly illuminated pixels compared with images with the mechanical X-ray shutter closed. The maximum and average integrated signal measured by the highly illuminated pixels in storage elements C_{S5} through C_{S8} were <0.02% and <0.004%, respectively, of the signal measured by storage elements C_{S1} through C_{S4} (both of which could be due to random variation).

Owing to an instability of the X-ray source (see below) it was not possible to use X-ray measurements to determine the time required to settle to high levels of accuracy. In a separate set of experiments an in-pixel circuit injected 235 fC, equivalent to 665 X-rays of 8 keV energy, into the pixel input and the time to settle to within particular levels of the final value was measured. The small-signal time constant and time for slew is longest for the smallest feedback capacitance; these times are reported here as a worst-case condition. The front-end amplifier transistor sizes were different on each half of the readout ASIC. This resulted in slightly different speeds for the two sides so that two settling times are reported for every measurement. At 15 μA dissipation by the front-end amplifier, amenable to a larger array, 10-bit settling (within 772 μV of the final value) required 100 and 80 ns and 12-bit settling (within 193 μV of the final value) required 120 and 90 ns. For the 16 × 16 device, per-pixel power dissipation is of less concern. At a larger power dissipation, 12-bit settling (within 193 μV of the final value) required 65 and 65 ns. With the 16 × 16 pixel device, 12-bit settling was shown possible at times required to segregate bunches at the APS or ESRF.

4.2. Beam characterization

The X-ray beam in the experimental hutch may have intensity and position fluctuations owing to trajectory instabilities of the electron/positron source or from motions of the optics that interact with the X-ray beam. Evaluation of these variations is important, particularly for time-resolved experiments. Diagnostics at or exceeding the frequencies of vibrations that may be driven by pumps are valuable for commissioning of X-ray beamlines.

The fast readout time of the PAD camera and the ability to resolve individual CHESS bunch trains allowed for unique characterization of the X-ray beam on microsecond time scales. Since the PAD directly images the beam on an array of pixels the beam profile is extracted, which provides more diagnostic information than four-quadrant-type beam-position monitors. The in-pixel storage was used to study temporal correlations of a train sampled at each pass around the synchrotron ring.

To characterize the stability of the X-ray beam each in-pixel storage element of the PAD captured a unique single pass of train five. The temporal separation between the capture of train five by each storage element was varied to study the time correlation of the position and intensity fluctuations. Each image read out from the detector measured the X-ray signal at multiple time differences, τ, because of the eight in-pixel storage elements. The time between PAD readout was limited to a minimum of 700 µs and varied from 719 µs to 2.7 ms to extract a range of time correlations.

The intensity, I, was measured as the sum of the entire spot; horizontal and vertical positions were found with a center-of-mass algorithm. The direct time evolution of the intensity and vertical position is shown in Fig. 9. Oscillations were detected at 100 Hz and 200 Hz and were discovered to be induced by vibrations of the monochromator from a vacuum pump.

To study faster time scales, intensity and position time correlations were evaluated by calculation of the average RMS deviation *versus* the time difference, τ, between the

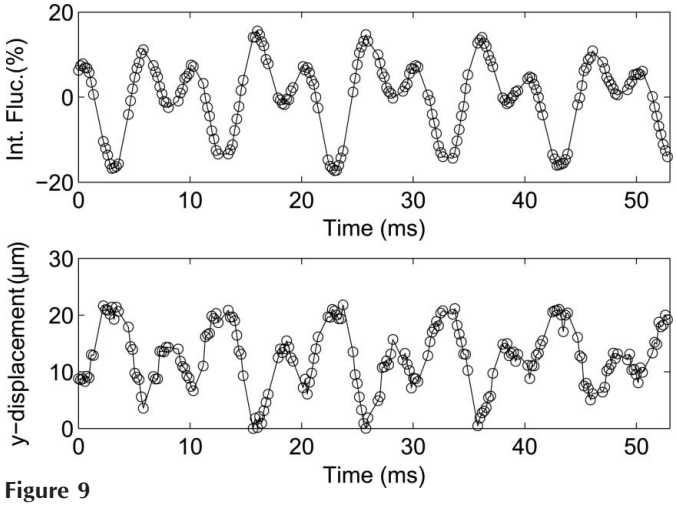

Figure 9
Millisecond time-scale studies of beam intensity fluctuations (top) and vertical displacement (bottom). For this measurement the detector waited for the fifth train to circulate the synchrotron 75 times between captures of the in-pixel storage elements. Lines are a guide to the eye.

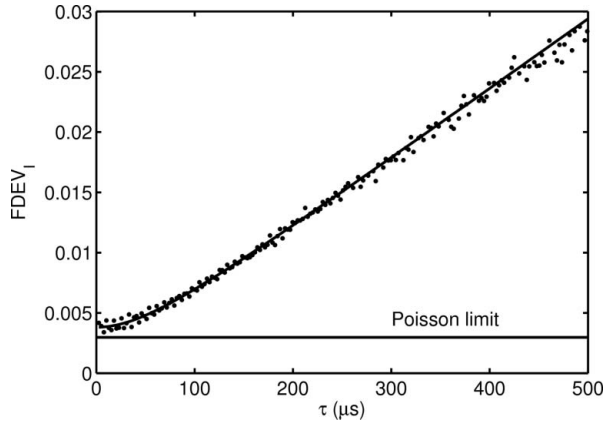

Figure 10
Fractional RMS fluctuation of the CHESS G3 beam intensity *versus* correlation time. The solid line is a fit to $\mathrm{FDEV}_\mathrm{I}^2 = A\tau^2 + P$.

measurements. This allowed for study down to the time of 2.56 µs for the train to circulate the ring. Fractional intensity deviations were evaluated as

$$\mathrm{FDEV}_\mathrm{I}(\tau) = \frac{\left\{\langle [I(t) - I(t+\tau)]^2 \rangle\right\}^{1/2}}{2^{1/2}\langle I \rangle},$$

where $\langle \ldots \rangle$ indicates an average. Horizontal deviations were calculated similarly, but not normalized to the average position, and indicated as $\mathrm{DEV}_X(\tau)$. The integrated intensity measured per capture was $\sim 1.1 \times 10^5$ X-rays which implies an accuracy limit from Poisson statistics for the intensity measure of $1/(1.1 \times 10^5)^{1/2} = 0.0030$.

Fig. 10 displays the fractional intensity deviations extracted for correlation times from 2.56 µs up to 500 µs. At the shortest correlation times the measurement is close to the accuracy limit set by Poisson statistics. To show this, the measured values were fit to $\mathrm{FDEV}_\mathrm{I}^2 = A\tau^2 + P$. The parameters found were: $A = (5.8 \times 10^{-5}\ \mu\mathrm{s}^{-1})^2$ and $P = 0.0038^2$ where P represents the deviation that is constant with correlation time and is bounded by Poisson statistics. Extraction of an almost Poisson limited measurement displays that the accuracy of the detector was maintained at high-flux levels and short exposure times. The linear growth of the intensity deviation with correlation time proves that the intensity fluctuations of the single train were dominated by the 100 Hz and 200 Hz oscillations shown in Fig. 9.

Fig. 11 displays the deviations of the center-of-mass of the X-ray intensity in the horizontal direction for correlation times up to 80 µs. The deviations oscillate at a frequency of 163 kHz which is attributed to betatron oscillations of the circulating positron cloud. The maximum sampling rate of this measurement was limited to the time for the train to circulate the ring. As such, it is not possible to determine whether the frequency extracted is the true frequency or an aliased measure of a higher frequency of the positron cloud motion. The actual possible transverse oscillation frequencies, f, are then 163 kHz = $|f - N \times 390.1\ \mathrm{kHz}|$ for any integer N (the revolution frequency at CHESS is 390.1 kHz). Before these experiments the horizontal betatron measurements were

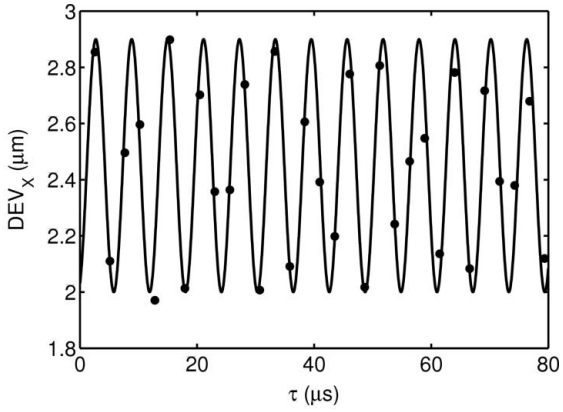

Figure 11
Fluctuations of the CHESS G3 beam horizontal position at fast time scales with a superimposed oscillation (solid line) at 163 kHz.

taken by the storage ring operators at a frequency of 227.7 kHz, which would be detected by the PAD as a frequency of $|227.7\ \text{kHz} - 390.1\ \text{kHz}| = 162.4$ kHz, consistent with measured results. These results show this detector to be appropriate for diagnostics of beam position and intensity fluctuations at, and exceeding, the typical frequencies of mechanical vibrations and many synchrotron ring instabilities.

5. Discussion

Pump–probe experiments use a laser to initiate dynamics in a sample which is then probed by an X-ray pulse with a known time delay with respect to the laser. The detector described would be a useful tool for these experiments. The detector readout time of 600 μs is faster than the typical repetition rate of the pump laser. The single-shot saturation value of the detector in a 1.2 mm × 1.4 mm spot was shown to exceed 10^5 X-rays. This large capacity maximizes the accuracy of time-resolved measurements that are limited by photon statistics. Another advantage is that, unlike a point detector, the two-dimensional pixel array provides sensitivity to peak position and profile for detection of lattice parameter shifts and lattice inhomogeneity. In-pixel storage elements may capture both the laser-on image and laser-off reference image in a single readout to reduce drifts.

This work will be leveraged for the planned development of a buttable larger format device for a wider range of time-resolved experiments. The pixel was designed with power dissipation appropriate for larger arrays. The FPGA control code developed benefits future larger arrays since the majority of the state machines are independent of detector format.

6. Conclusions

A strength of analog integrating PADs is the high-count-rate capability that minimizes uncertainty due to Poisson statistics at short exposure times. In this paper an analog integrating area detector was demonstrated with speed sufficient to segregate X-ray signals separated by around 150 ns onto in-pixel storage elements. This time resolution is appropriate for the 176 ns bunch separation in 16 bunch mode at the ESRF, the 153 ns bunch separation in a standard operating mode at the APS, and the 150 ns pulse spacing at the European XFEL (Graafsma, 2009). The PAD was applied to studies of turn-by-turn X-ray bunch-train intensity and horizontal position measurements at correlation times down to 2.56 μs. Single Bragg spot time-resolved studies, especially of non-repetitive sample dynamics, are an excellent experimental match for future applications.

The authors acknowledge the Cornell detector group for their support: Darol Chamberlain, Katherine S. Green, Marianne S. Hromalik, Hugh Philipp and Mark W. Tate; Martin Novak for machining of the enclosure; Arthur Woll, Tushar Desai, John Ferguson and Katherine S. Green for help at the beamline. We are also grateful to Tom Hontz and Area Detector Systems Corporation (ADSC) for the high-resistivity detector chips. This work was supported by the William M. Keck foundation and DOE-BER Grant DE-FG02-97ER62443. CHESS is supported by the US NSF and NIH-NIGMS through NSF grant DMR-0225180.

References

Anelli, G., Campbell, M., Delmastro, M., Faccio, F., Floria, S., Giraldo, A., Heijne, E., Jarron, P., Kloukinas, K., Marchioro, A., Moreira, P. & Snoeys, W. (1999). *IEEE Trans. Nucl. Sci.* **46**, 1690–1696.
Baron, A. Q. R., Rüffer, R. & Metge, J. (1997). *Nucl. Instrum. Methods Phys. Res. A*, **400**, 124–132.
Cammarata, M., Eybert, L., Ewald, F., Reichenbach, W., Wulff, M., Anfinrud, P., Schotte, F., Plech, A., Kong, Q., Lorenc, M., Lindenau, B., Rabiger, J. & Polachowski, S. (2009). *Rev. Sci. Instrum.* **80**, 015101.
Cheong, S.-K., Liu, J., Powell, C. F. & Wang, J. (2004). *AIP Conf. Proc.*, **705**, 961–964.
Clayton, J. E., Chen, C. M. H., Cook, W. R. & Harrison, F. A. (2003). *2003 IEEE Nuclear Science Symposium Conference Record*, Vol. 5.
DeCamp, M. F., Reis, D. A., Fritz, D. M., Bucksbaum, P. H., Dufresne, E. M. & Clarke, R. (2005). *J. Synchrotron Rad.* **12**, 177–192.
Ejdrup, T., Lemke, H. T., Haldrup, K., Nielsen, T. N., Arms, D. A., Walko, D. A., Miceli, A., Landahl, E. C., Dufresne, E. M. & Nielsen, M. M. (2009). *J. Synchrotron Rad.* **16**, 387–390.
Ercan, A., Tate, M. W. & Gruner, S. M. (2006). *J. Synchrotron Rad.* **13**, 110–119.
Graafsma, H. (2009). *J. Instrum.* **4**, P12011.
Henrich, B., Becker, J., Dinapoli, R., Goettlicher, P., Graafsma, H., Hirsemann, H., Klanner, R., Krueger, H., Mazzocco, R., Mozzanica, A., Perrey, H., Potdevin, G., Schmitt, B., Shi, X., Srivastava, A., Trunk, U. & Youngman, C. (2010). *Nucl. Instrum. Methods Phys. Res. A*, doi:10.1016/j.nima.2010.06.107.
Koerner, L. J. (2010). PhD thesis, Cornell University, USA.
Koerner, L. J., Tate, M. W. & Gruner, S. M. (2009*b*). *IEEE Trans. Nucl. Sci.* **56**, 2835–2842.
Koerner, L., Philipp, H., Hromalik, M., Tate, M. & Gruner, S. (2009*a*). *J. Instrum.* **4**, P03001.
Nüske, R., Schmizing, C. K., Jurgilaitis, A., Enquist, H., Navirian, H., Sondhauss, P. & Larsson, J. (2010). *Rev. Sci. Instrum.* **81**, 013106.
Rossi, G., Renzi, M., Eikenberry, E. F., Tate, M. W., Bilderback, D., Fontes, E., Wixted, R., Barna, S. & Gruner, S. M. (1999). *J. Synchrotron Rad.* **6**, 1096–1105.
Snoeys, W., Gutierrez, T. & Anelli, G. (2002). *IEEE Trans. Nucl. Sci.* **49**, 1829–1833.
Trenkle, J. C., Koerner, L. J., Tate, M. W., Gruner, S. M., Weihs, T. P. & Hufnagel, T. C. (2008). *Appl. Phys. Lett.* **93**, 081903.
Wong, H. (1996). *IEEE Trans. Electron Dev.* **43**, 2131–2142.